Advanced Three-Dimensional Tailored RF Pulse for Signal Recovery in T_2^*-Weighted Functional Magnetic Resonance Imaging

Chun-yu Yip,[1]* Jeffrey A. Fessler,[1,2] and Douglas C. Noll[2]

T_2^*-weighted functional MR images are plagued by signal loss artifacts caused by susceptibility-induced through-plane dephasing. We present major advances to the original three-dimensional tailored RF (3DTRF) pulse method that precompensates the dephasing using three-dimensional selective excitation. The proposed 3DTRF pulses are designed iteratively with off-resonance incorporation and with a novel echo-volumar trajectory that frequency-encodes in *z* and phase-encodes in *x*, *y*. We also propose a computational scheme to accelerate the pulse design process. We demonstrate effective signal recovery in a 5-mm slice in both phantom and inferior brain, using 3DTRF pulses that are only 15.4 ms long. Compared to the original method, the new approach leads to significantly reduced pulse length and enhancement in slice selectivity. 3D images of the slice volume confirm fidelity of the excited phase pattern and slice profile. Magn Reson Med 56:1050–1059, 2006. © 2006 Wiley-Liss, Inc.

Key words: signal recovery; signal loss; functional MRI; three-dimensional tailored RF pulse; echo-volumar trajectory

Blood-oxygenation-level-dependent T_2^* contrast for functional MRI (fMRI) originates from mesoscopic magnetic spin dephasing. Unfortunately, T_2^* contrast is coupled to signal loss artifacts due to dephasing caused by macroscopic inhomogeneity of the main field. A major cause of macroscopic field inhomogeneity in the human head is the bulk magnetic susceptibility (BMS) differences across the interface between tissue and air-filled cavities, such as the sinuses. During the long echo time (T_E) required for T_2^* contrast, an inhomogeneous field causes intravoxel spin signal dephasing and consequently phase cancellation during readout leads to signal loss. This signal loss artifact hampers fMRI studies of brain regions proximal to air cavities, such as the orbital frontal and inferior temporal cortices (1).

Various techniques have been proposed to recover the BMS-induced lost signals, but they have different drawbacks. One class of methods focuses on optimization of slice and acquisition parameters (2–6). These methods generally recover signals only partially, and they interfere with brain coverage preferences that are specific to the functional study. Refs. (7–9) proposed compensation of the dephasing using extra gradient lobes. To achieve acceptable recovery, these methods generally require multiple scans for one slice location, leading to loss of temporal resolution of the fMRI experiment. Inspired by the tailored RF pulse method that creates quadratic through-plane phase variation (uniform in-plane) for excitation-stage partial "precompensation" of the dephasing (10), Ref. (11) proposed using three-dimensional TRF (3DTRF) pulses for phase precompensation with in-plane selectivity. However, those pulses are undesirably long and thus compromise temporal resolution as well. On the acquisition side, using spiral in–out (12) or spiral in–in (13) trajectories recovers some signals compared to the spiral-out case, but recovery is usually partial. Last, it has also been demonstrated that intraoral and external localized shimming (14–16) can effectively improve field homogeneity and recover signals. However, placement of extra hardware may lead to subject discomfort and may not be appropriate for use with children or psychiatric patients.

Among these solutions, the method of using 3DTRF pulses for phase precompensation (hereafter, the 3DTRF method) deserves further development for full realization of its potential. The method has several advantages. It does not interfere with imaging parameters such as voxel size or slice orientation, nor does it require multiple subimage acquisition for a single image, and thus multifold temporal resolution loss is avoided. The method also obviates placement and calibration of extra shimming hardware. Finally, 3DTRF pulses can be applied in conjunction with the other methods to further improve signal recovery.

Although the long duration of 3DTRF pulses could potentially be reduced by the emerging parallel transmission technology (17, 18), pulse length reduction should be the primary focus of new approaches to the 3DTRF method, because it is related directly to fMRI temporal resolution. Furthermore, new approaches should aim to improve excitation accuracy, which affects signal recovery efficacy and slice selection fidelity. To accomplish this, off-resonance effects *during* pulse deployment must be considered, because 3DTRF pulses are long and applied in brain regions with severe field inhomogeneity.

In this article we introduce an advanced approach to the 3DTRF method, comprising a novel trajectory in 3D excitation *k*-space (19), and new pulse design procedures. The proposed trajectory provides better *k*-space sampling efficiency, leading to significantly shorter pulses. It also provides slice profiles that are less susceptible to off-resonance distortion. The 3DTRF pulses are designed *iteratively* (20), incorporating resonance frequency offsets measured in a separate scan.

[1]Department of Electrical Engineering and Computer Science, University of Michigan, Ann Arbor, Michigan.

[2]Department of Biomedical Engineering, University of Michigan, Ann Arbor, Michigan.

Grant sponsor: NIH; Grant number: DA15410.

*Correspondence to: Chun-yu Yip, Functional MRI Laboratory, University of Michigan, 2360 Bonisteel Avenue, Ann Arbor, MI 48109-2108, USA. E-mail: chunyuy@umich.edu

Received 19 April 2006; revised 11 July 2006; accepted 12 July 2006.

DOI 10.1002/mrm.21048

Published online 13 October 2006 in Wiley InterScience (www.interscience.wiley.com).

For in vivo signal recovery, 3DTRF pulses must be computed *online* during an fMRI session. However, the 3D off-resonance-incorporated pulse design problem can be computationally demanding. To accelerate the design process, we propose a computational scheme analogous to the so-called *time* and *frequency segmentation* methods in image reconstruction (21–24). It makes the 3DTRF method potentially practical for routine fMRI experiments.

THEORY

Synopsis of the 3DTRF Method

Assuming a 2D imaging scheme, let x,y denote the in-plane dimensions and z the slice selection direction. Define $\mathbf{r} = (x, y, z)$, and let $\Delta B(x, y, z)$ denote the BMS-induced inhomogeneous field. When imaging at slice location z_0, the through-plane differential phase variation at in-plane location (x, y) responsible for signal loss can be described by

$$\phi(x, y, z; z_0) = -\gamma T_E[\Delta B(x, y, z) - \overline{\Delta B}(x, y; z_0)], \quad [1]$$

where γ is the gyromagnetic ratio, and $\overline{\Delta B}(x, y; z_0)$ are the mean field offsets around z_0 in the through-plane direction, defined by

$$\overline{\Delta B}(x, y; z_0) = \frac{\int p(z - z_0)\Delta B(x, y, z)dz}{\int p(z - z_0)dz}, \quad [2]$$

where $p(z)$ is the slice profile. The mean offsets cause in-phase evolution of spin signals and therefore do not contribute to through-plane dephasing. For T_2^* contrast, T_E must be relatively long (typically 30–50 ms), and consequently this phase variation is rapid in regions with large field variation. MR signals that originate from integration of spins in those regions are lost due to phase cancellation during readout.

The goal of the 3DTRF method (11) is to *precompensate* for this through-plane phase variation in the excitation stage. In the ideal case, a 3DTRF pulse excites a slice-selective volume, d, with the negative of the phase pattern in Eq. [1] embedded:

$$d(\mathbf{r}; z_0) = p(z - z_0) \cdot \exp[-\imath\phi(x, y, z; z_0)], \quad [3]$$

where $\imath = \sqrt{(-1)}$.

This preemptive phase pattern, if realized, would cancel out the through-plane dephasing during T_E, and spins would be in phase when the center of acquisition k-space is sampled at T_E. Signal loss would thus be mitigated. Although the 3DTRF method described here precompensates only for through-plane dephasing, generalization for in-plane dephasing correction may be possible.

Iterative Design of 3DTRF Pulses

Selective excitation of 3D patterns is facilitated by the excitation k-space concept, under small-tip-angle approximation of the Bloch equation (19). Using the k-space formulation, the 3DTRF pulse for a given k-space trajectory can be designed iteratively with high efficiency (20). To do this, one must first specify the discrete *desired pattern* by sampling the ideal one, $d(\mathbf{r}; z_0)$, over a 3D Cartesian grid. We discuss criteria for adequate sampling of $d(\mathbf{r}; z_0)$ under Materials and Methods.

Let $d_i = d(\mathbf{r}_i; z_0), i = 0, \ldots, N_s - 1$ be the desired pattern samples over a 3D Cartesian grid, and define complex vector $\mathbf{d} = (d_0, \ldots, d_{N_s-1})$. Based on (20), complex 3DTRF pulse samples, $\hat{\mathbf{b}} = (\hat{b}_0, \ldots, \hat{b}_{N_t-1})$, can be designed via solving the following unconstrained minimization problem:

$$\hat{\mathbf{b}} = \arg\min_{\mathbf{b}} \left\{ \|\mathbf{Ab} - \mathbf{d}\|_{\mathbf{W}}^2 + R(\mathbf{b}) \right\}, \quad [4]$$

where $\mathbf{A}$ is an $N_s \times N_t$ *system matrix* with elements

$$a_{i,j} = \imath\gamma e^{\imath\mathbf{k}(t_j)\cdot\mathbf{r}_i + \imath\Delta\omega(\mathbf{r}_i)[t_j - T]}\Delta t, \quad i = 0, \ldots, N_s - 1, j = 0, \ldots, N_t - 1, \quad [5]$$

in which $\mathbf{k}(t_j)$ is the excitation k-space location at time t_j determined by backward integration of the applied gradient waveforms (19), Δt is the pulse sampling interval, T is the pulse duration, and $\Delta\omega(\mathbf{r}_i)$ is the resonance frequency offset at $\mathbf{r}_i$. The $N_s \times N_s$ diagonal matrix $\mathbf{W}$ contains error weights, $W_i, i = 0, \ldots, N_s - 1$, that we can devise to specify regions of interest (ROIs) and "don't-care" regions (20). $\mathbf{Ab}$ approximates the pattern excited by $\mathbf{b}$, and with the first term in the cost function in Eq. [4] we seek to minimize its difference from $\mathbf{d}$ in a weighted least-squares sense. $R(\mathbf{b})$ is a penalty function that, if defined as $\beta\mathbf{b}'\mathbf{b}$ and $\mathbf{b}'\mathbf{\Lambda b}$, can be used to control integrated and instantaneous RF pulse power, respectively (20). These power penalties can be tuned through parameters β and $\mathbf{\Lambda} = diag\{\lambda_j\}, j = 0, \ldots, N_t - 1$. The minimization problem can be solved iteratively using the efficient conjugate gradient (CG) algorithm (20).

Incorporating off resonance effects in the design (Eq. [5]) is crucial in context of the 3DTRF method, because the pulses are relatively long and are deployed in brain regions with severe field inhomogeneity. Unfortunately, in doing so, the Fourier relationship between excitation pattern and k-space is ruined. The efficient fast Fourier transform (FFT) cannot be used directly in mappings between excitation pattern and k-space, as needed in CG (24). Acceleration techniques are needed for the computational time of the design problem to be practical, as addressed in a subsequent section.

An Echo-Volumar Trajectory

The effectiveness of an RF pulse designed via Eq. [4] depends greatly on the choice of k-space trajectory in Eq. [5]. For sampling efficiency and excitation accuracy, we can tailor an appropriate 3D trajectory for the 3DTRF method. The method imposes high demands in the slice selection direction. The 3DTRF pulses must have excitation FOV (XFOV) in z wide enough to cover the range over which MR signals can arise and excitation resolution fine enough for rendering rapid phase variations and narrow slice profiles. In contrast, the in-plane requirements are relatively less stringent, because in-plane excitation resolution can be low due to the smooth in-plane variation of the desired pattern. The stack-of-spirals trajectory in Ref. (11), which "phase-encodes" in z and "frequency-encodes" in x, y, is suboptimal for the 3DTRF method. While it can efficiently support high in-plane XFOV and resolution, it is inefficient in meeting demanding z-direction requirements. Also, phase-encoding in z produces slice profiles vulnerable to off-resonance distortion.

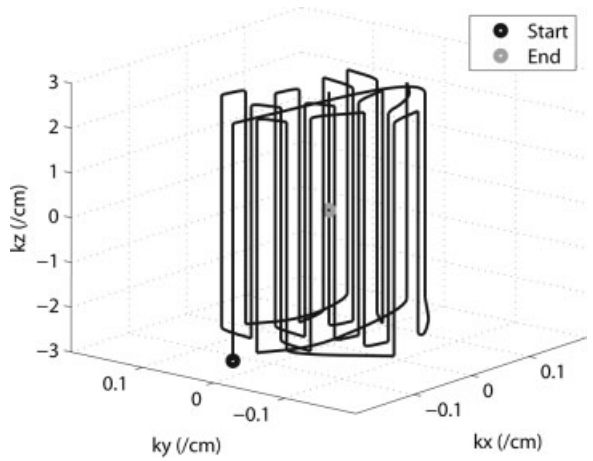

FIG. 1. EV trajectory in 3D excitation k-space, used in the phantom experiment. It frequency encodes in the slice-selection direction and phase encodes in-plane.

We propose a novel trajectory in 3D excitation k-space that frequency-encodes in z and phase-encodes in x, y (Fig. 1). It traverses back and forth along the k_z direction. Such traversal can be produced by an oscillative z gradient waveform, subject to the maximum gradient magnitude and slew rate constraints (Fig. 2a). The oscillative z gradient can be trapezoidal, sinusoidal, or of any other shape so long as it provides the desired oscillative k_z locus. In between the forward and backward k_z traversals, x and y gradient blips are deployed to take the trajectory to predetermined phase-encoding locations in k_x, k_y (Fig. 2a). As a result, the 3D trajectory cyclically sweeps k_z (in either positive or negative direction) at a particular k_x, k_y location and then migrates to another one. The cycle continues until the trajectory visits $k_x, k_y = (0, 0)$ and finally lands on the origin of excitation k-space. Such a 3D trajectory resembles the one used in blipped echo-volumar imaging (25) and hence we coin it an echo-volumar (EV) trajectory, as extension of the echo-planar trajectories in the pulse design literature (for example, (26)).

The EV trajectory eliminates the problem of "excitation sidelobes" in the z direction as reported in Ref. (11), because during the k_z traversals, RF and z gradient waveforms are essentially played out "continuously" in the coils after digital-to-analog conversion. Frequency-encoding in z also enables efficient coverage of a wide k_z range, which directly leads to significant pulse length reduction. It also provides slice profiles that are less vulnerable to off-resonance distortion.

Determination of Phase-Encoding Locations

Using a fine Cartesian grid of phase-encoding locations in k_x, k_y would be an inefficient sampling strategy that leads to lengthy pulses. Instead, we pick a modest set of locations, judiciously chosen to help minimize the cost function in Eq. [4]. The trajectory can adapt to the desired pattern by traversing the highest energy regions of its spectrum in excitation k-space. One intuitive strategy is to set the N phase-encoding locations to be the k_x, k_y coordinates corresponding to the N largest values in the desired pattern's discrete k_x, k_y power spectrum, obtained via collapsing the 3D power spectrum along the k_z dimension:

$$E(k_{x,i}, k_{y,j}) = \sum_{k=0}^{N_z-1} |D(k_{x,i}, k_{y,j}, k_{z,k})|^2, \quad i = 0, \ldots, N_x - 1, j = 0, \ldots, N_y - 1, \quad [6]$$

where D denotes the 3D discrete Fourier transform of the adequately sampled desired pattern, and N_x, N_y, and N_z are the numbers of samples in the three spatial dimensions.

When off resonance is incorporated in the design process, determining the locations based on the power spectrum of the following "modified desired pattern" generally leads to lower cost (Fig. 3):

$$\tilde{d}_i = d_i \cdot e^{\iota \Delta\omega(\mathbf{r}_i)T}, \qquad i = 0, \ldots, N_s - 1. \quad [7]$$

This modification partially accounts for the off-resonance phase evolution during pulse deployment and leads to better choice of phase-encoding locations. Further optimization of the encoding locations is currently under investigation.

In the presence of field inhomogeneity, ordering of the trajectory's visit to phase-encoding locations critically affects excitation accuracy. The crucial encoding locations at k-space center ($k_x, k_y = (0, 0)$) and its proximity should be visited last, so that dephasing and decay of those encoding components is minimized. The EV trajectory can therefore "spiral in" from the high-frequency region toward the center (Fig. 3). Such ordering also leads to relatively

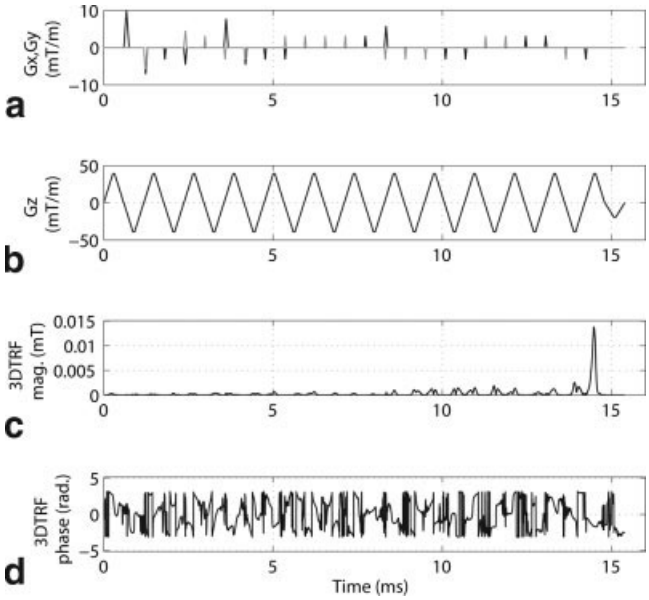

FIG. 2. 3DTRF pulse used in the phantom experiment. **a:** x- (black) and y- (gray) gradient waveforms that produce the k_x, k_y displacements of the EV trajectory in Fig. 1. **b:** z-gradient waveform that produces the k_z sweeps. **c,d:** 3DTRF pulse (magnitude and phase) iteratively designed with the trajectory in Fig. 1. The magnitude spike close to pulse end corresponds to the trajectory's visit to excitation k-space origin. This 3DTRF pulse is 15.4 ms long.

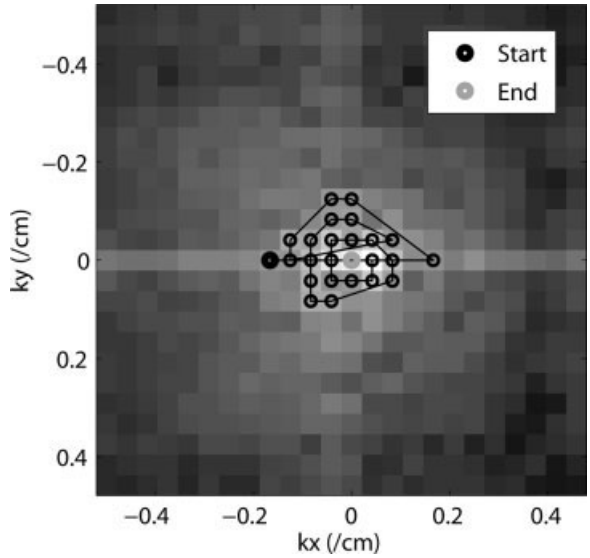

FIG. 3. Phase-encoding locations in k_x, k_y determined as the locations corresponding to the highest magnitudes in the discrete k_x, k_y power spectrum (underlying, in logarithmic gray scale) of the "modified desired pattern." They are visited by the EV trajectory, which traverses back and forth along k_z, in a "spiral-in" order (solid line).

good off-resonance resilience of the resulting excitation pattern.

Accelerating the Iterative Design

Motivation for Fast Computation

In an fMRI session, 3DTRF pulses for loss-plagued slice locations must be designed *online* after a separate scan for map of frequency offsets (hereafter field map). Therefore, the design process must be reasonably fast. However, solving Eq. [4] (with non-zero field map) using CG is computationally demanding, especially in the 3D case with large numbers of desired pattern and pulse samples.

The computational bottleneck in each CG iteration is the evaluation of products $\mathbf{A}'\mathbf{e}^{(n)}$, where $\mathbf{e}^{(n)} = \mathbf{d} - \mathbf{A}\mathbf{b}^{(n)}$ and $\mathbf{A}\mathbf{b}^{(n)}$ (superscript (n) denotes the nth iteration). When a field map is not incorporated in $\mathbf{A}$ (i.e., $\Delta\omega(\mathbf{r}_i) = 0$), these multiplications can be computed efficiently with the nonuniform fast Fourier transform (NUFFT) algorithm and its adjoint, respectively (27). NUFFT involves an $O(\kappa N_s \log N_s)$ FFT and an $O(JN_t)$ interpolation at its core, whereas its adjoint involves $O(JN_t)$ interpolation followed by $O(\kappa N_s \log N_s)$ inverse FFT. Here, J is the number of neigboring samples used in interpolation, and κ is the upsampling factor of spatial samples (27). The NUFFT algorithm and its adjoint provide a huge computation saving when compared to the $O(N_s N_t)$ exact evaluation of the matrix–vector products. However, when field map is incorporated, matrix $\mathbf{A}$ is no longer a Fourier transformation matrix. As a consequence, the fast algorithms cannot be used directly.

An analogous computational issue has been well addressed in the context of off-resonance-compensated image reconstruction. Using the *time segmentation* (22, 24) and *frequency segmentation* (21,23) methods, reconstruction is sped up significantly via approximations to the frequency offset exponential term in the magnetic resonance signal equation, and the subsequent use of the efficient (NU)FFT algorithm. These segmentation methods, in the context of CG-based reconstruction, have recently been generalized in (28). The analogy between reconstruction and small-tip-angle pulse design suggests that similar segmentation techniques can be applied to accelerate the 3DTRF pulse design process.

Framework of Segmentation for Pulse Design

Based on (28), all of the known approximations to the off-resonance exponential term in Eq. [5] are special cases of the following general form:

$$e^{\imath\,\Delta\omega(\mathbf{r}_i)t_j} \approx \sum_{l=1}^{L} p_{il} q_{lj}, \qquad i = 0, \ldots, N_s - 1, j = 0, \ldots, N_t - 1 \quad [8]$$

for various choices of the L pairs of spatial and temporal functions, $\{p_{il}, q_{lj}\}, l = 1, \ldots, L$. L is the number of "segments," which determines the approximation accuracy. Note that the exponent in Eq. [8] has positive sign, and the space and k-space indices are swapped, in contrast to that in the MR signal equation. Reference (28) describes methods for choosing p_{il} and q_{lj}, corresponding to the temporal interpolators and segments in the time segmentation method, and frequency segments and interpolators in frequency segmentation. In particular, the *histogram-based, least-square time segmentation* approach (28) is summarized in the Appendix.

Consider the formula of multiplying $\mathbf{A}$ with generic RF pulse vector $\mathbf{b}$. After substituting Eq. [8] into Eq. [5] and rearranging, the ith element of the product is

$$[\mathbf{A}\mathbf{b}]_i \approx \imath\gamma\Delta t \cdot e^{-\imath\,\Delta\omega(\mathbf{r}_i)T} \cdot \sum_{l=1}^{L} p_{il} \left[\sum_{j=0}^{N_t-1} (q_{lj} b_j) e^{\imath\,\mathbf{k}(t_j)\cdot\mathbf{x}_i} \right] \quad [9]$$

and in matrix form

$$\mathbf{A}\mathbf{b} \approx \mathbf{S} \cdot \sum_{l=1}^{L} \mathbf{P}_l \mathbf{G} \mathbf{Q}_l \mathbf{b}, \quad [10]$$

where $\mathbf{P}_l = diag\{p_{il}\}$, $\mathbf{Q}_l = diag\{q_{lj}\}$, $\mathbf{G}$ is an $N_s \times N_t$ adjoint NUFFT matrix with elements $g_{ij} = e^{\imath\,\mathbf{k}(t_j)\cdot\mathbf{x}_i}$, and $\mathbf{S} = diag\{\imath\gamma\Delta t \cdot e^{-\imath\,\Delta\omega(\mathbf{r}_i)T}\}$. Equation [10] depicts the following steps in approximating the multiplication:

1. For $l = 1, \ldots, L$:
   (a) multiply RF pulse samples with $q_{lj}, j = 0, \ldots, N_t - 1$;
   (b) apply adjoint NUFFT to $q_{lj} b_j$;
   (c) multiply adjoint NUFFT output with $p_{il}, i = 0, \ldots, N_s - 1$.
2. Sum the output of the L data branches.
3. Multiply the sum by $\imath\gamma\Delta t \cdot e^{-\imath\,\Delta\omega(\mathbf{r}_i)T}$.

This procedure is illustrated in Fig. 4. It can be handled efficiently using L adjoint NUFFT calls and with good choices of p_{il} and q_{lj}, a small L (4–8 for typical field maps in human head) is usually sufficient for the approximation in Eq. [9] to be accurate. Therefore, this procedure is significantly faster than the $O(N_s N_t)$ direct implementation

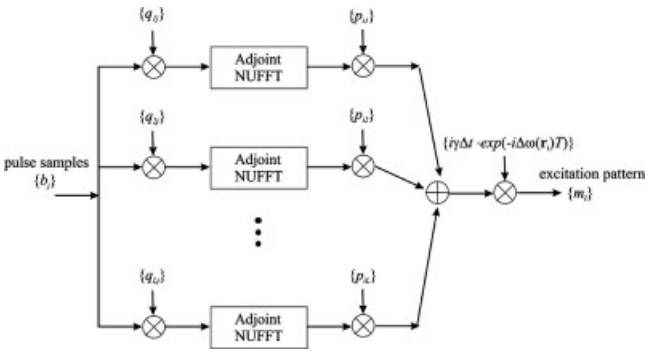

FIG. 4. Segmentation framework for fast and accurate approximation of generic $\mathbf{m} = \mathbf{Ab}$.

of $\mathbf{Ab}$. Similarly, multiplication of $\mathbf{A}'$ with generic spatial vector $\mathbf{e}$ can be approximated with L NUFFT calls. The complexity reductions in each CG iteration lead to significant acceleration of the 3DTRF pulse design process.

MATERIALS AND METHODS

In this section, we elaborate on the field map acquisition and implementation of the 3DTRF pulse design process. We also give parameter values used in the experiments presented in the subsequent section.

Scanning for Field Map

To acquire a field map, we perform a separate scan, in which we obtain two multislice 2D gradient-echo (GRE) image sets with an echo time difference, ΔT_E (29). ΔT_E should be small enough so that no phase evolution during the period exceeds $\pm\pi$. The field map, in Hertz, can be estimated by dividing the phase difference between the two image sets by $2\pi\Delta T_E$. The prescribed slices should be thin and dense enough to capture the phase variations through the target slices in the actual fMRI study. In-plane resolution can be relatively low. FOV in z should cover the slice locations where 3DTRF pulses are targeted. In fact, field map coverage larger than the target range is beneficial for off resonance compensation in the design. To exclude fat signals from the pulse design process, we apply fat presaturation to attenuate the fat signals, threshold the magnitude images to obtain masks covering only the brain, and then apply the masks to crop out the fat regions in the field map (i.e., assign 0 Hz everywhere except within the brain). The masked map is to be smoothed in the next step.

In our phantom and human experiments, the field map was acquired with a 2D GRE spiral-out sequence, with common parameters as follows: slice thickness = 0.1 cm, number of slices = 40, flip angle = 60°, FOV = 24 cm, matrix size = 64×64, $T_R = 2$ s, $T_E = 6.8$ ms, number of interleaves = 4, and $\Delta T_E = 1$ ms.

3DTRF Pulse Design

Figure 5 summarizes the 3DTRF pulse design process with the field map and its associated magnitude images as input. First, we apply regularized in-plane smoothing to the masked field map (30). The procedure denoises the field map and extrapolates it into image gaps and background. We then smooth the field map in the z direction with a 1D Hanning kernel. We smooth the magnitude images, which will be used to determine the ROI, with a 2D Hanning kernel. This smoothing ensures that the ROI covers brain regions with low signal intensities. We subsequently interpolate the smoothed field map and magnitude images onto the lattice grid on which the desired pattern will be specified.

There are several considerations in choosing the desired pattern grid. First, the sampling rates in each spatial dimension should at least match the spatial frequency bandwidth of the continuous desired pattern (Eq. [3]). Therefore, sampling in z should be fine because of the rapid through-plane phase variation and narrow slice profile, whereas coarser sampling in x, y is allowable, because usually the phase of the desired pattern is smooth in-plane. Second, the sampling ranges in the three dimensions must cover the entire volume of interest, implying that the grid has to cover a wide range of z from which MR signals can arise.

Sampling parameters of the desired pattern in our experiments are as follows: FOV = 24×24 $(x, y) \times 12.8$ cm (z), with spacings 1×1 $(x, y) \times 0.1$ cm (z).

Desired Pattern Specification

For each slice targeted for recovery, we select a set of processed 2D field maps corresponding to the subslices that constitute the target slice. From these field maps, the complex desired pattern is formed based on the discretized version of Eqs. [1], [2], and [3]. T_E is defined as the interval between pulse end and time of acquisition k-space

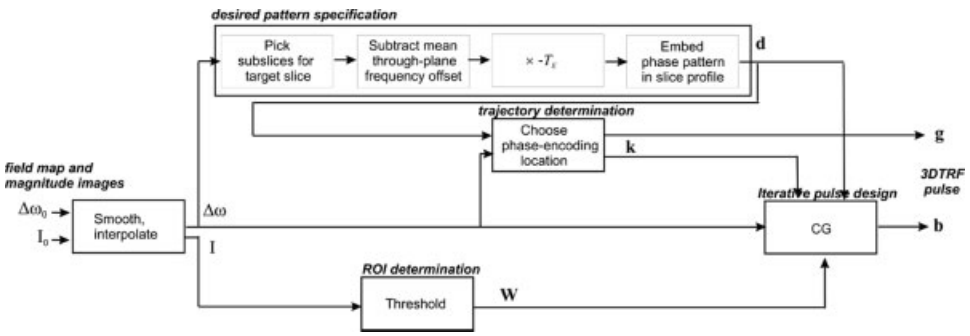

FIG. 5. Flowchart of the 3DTRF pulse design process, with field map and corresponding magnitude images as input.

origin. We assign zeros to desired pattern grid locations outside the slice volume. Finally, regardless of the target slice location, the desired pattern can be specified centered in the z dimension. Slice placement off the iso-center can be achieved by frequency modulation implementable in the pulse sequence.

In both of our experiments, the desired pattern had Gaussian-shape slice profile with full-width half maximum (FWHM) = 0.5 cm and tip angle = 30°. $T_E = 30$ ms.

Trajectory and ROI Determination

One can now proceed to determine the k-space trajectory based on the field map and desired pattern. We determine the phase-encoding locations from the spectrum of the modified desired pattern (Eq. [7]). The trajectory's k_z coverage should be large enough for the required slice thickness and through-plane phase variation. Thresholding the interpolated magnitude images will generate the ROI that covers the brain where excitation accuracy is important. This threshold should be lower than the one for fat region exclusion, so that brain regions with low signal intensity are included in the ROI.

In our experiments, gradient trapezoids were compliant to the maximum gradient magnitude and slew rate constraints, which were 40 mT/m and 150 T/m/s, respectively. We used 25 phase-encoding locations and k_z coverage of $[-2.65, +2.65]\,\text{cm}^{-1}$, resulting in pulse length = 15.4 ms. We adopted a "spiral-in" ordering of the phase-encoding locations as illustrated in Fig. 3.

Iterative Pulse Design

After determining the field map, desired pattern, trajectory, and ROI, we design the 3DTRF pulse iteratively with CG, implemented with Matlab (The Mathworks, Inc., Natick, MA, USA) on a 3.2-MHz Pentium workstation. We apply Tikhonov regularization (with small β) to avoid unrealizable pulse designs. In the case of pulse power violation in the final design, one can cyclically increment regularization parameters (β and $\mathbf{\Lambda}$) and run extra CG iterations (20) until pulse power is within acceptable range. In the experiments presented here, we added an *ad hoc* penalty function of the form $\alpha\mathbf{b}' \cdot diag\{k_x(t_j)^2 + k_y(t_j)^2\} \cdot \mathbf{b}$ to Eq. [4], which smoothed the in-plane excitation pattern. Similar to β and $\mathbf{\Lambda}$, α is a design parameter. To accelerate the design as proposed, we precompute temporal interpolators for the segmentation scheme as described in the Appendix and NUFFT interpolators based on (27). The interpolators are stored and utilized in each CG iteration.

The 3DTRF pulses in our experiments were designed with 50 CG iterations, $\beta = 1$, $\lambda_i = 0$, all i, and $\alpha = 5000$ (with trajectory samples in cm^{-1}). RF pulse computation was accelerated with the histogram-based, least-squares time segmentation method as described in the Appendix. There were 8 bins in the field map histogram ($K = 8$), and 4 temporal segments at uniform intervals ($L = 4$). For the NUFFT algorithm (27), we used 4 neighbors for interpolation ($J = 4$), an upsampling factor of 2 ($\kappa = 2$), in all three dimensions.

The outputs of the design process are magnitude and phase waveforms for the RF envelope to be frequency modulated, accompanied by gradient waveforms underlying the 3D trajectory. These waveforms are incorporated into the pulse sequence.

Scanner Experiments

Scanner experiments were conducted on a GE 3-T Excite MRI scanner (GE Healthcare, Milwaukee, WI, USA), with a head coil for both transmission and reception. Our phantom experiment was performed on a spherical homogeneous water phantom. A healthy volunteer participated in the human experiment, approved by the Institutional Review Board of the University of Michigan, after providing informed consent. In both phantom and human experiments, we performed high-order shimming prior to field map acquisition. Gradient and RF waveforms were shifted slightly to compensate for delays between the RF and gradient channels. We reconstructed 2D images using the off-resonance-compensated conjugate-phase method (22).

Signal Recovery in Phantom

The goals of the experiment are (1) to demonstrate signal recovery using a 3DTRF pulse in a homogeneous water phantom; (2) to image the slice volume excited by that 3DTRF pulse, using a 3D imaging sequence. With the slice volume image, we evaluated fidelity of the magnitude and phase profiles of the excited slice.

To induce an inhomogeneous field, we attached a small piece of ferromagnetic metal (half piece of staple) on the phantom surface, 6 cm inferior to the imaging plane at isocenter. The created inhomogeneous field led to signal loss in a GRE image at iso-center, acquired with a conventional 3.2-ms-long, Hanning-windowed, sinc-shape (with 1 sidelobe) RF pulse that was selective for a 5-mm slice. The other imaging parameters were as follows: spiral-out acquisition with matrix size 128 × 128, FOV = 24 cm, 8 interleaves, $T_E = 30$ ms, $T_R = 1$ s, and flip angle = 30° (matched with the 3DTRF case). The use of small pixel size and multiple interleaves minimized image artifacts due to in-plane dephasing and the phase error during acquisition. Therefore, through-plane dephasing was the dominant cause of signal loss.

We subsequently attempted to recover the lost signals with a 3DTRF pulse. We scanned the phantom for field map and designed a 3DTRF pulse, as described above. The sinc pulse in the GRE sequence was replaced by the 3DTRF pulse, with the same imaging parameters. The image acquired with the 3DTRF pulse was compared with that acquired using the sinc pulse.

In a separate scan, with metal still attached and shim values unchanged, we imaged the slice volume excited by

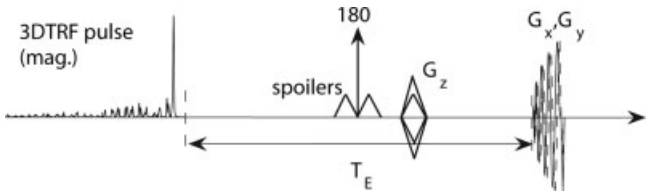

FIG. 6. Spin-echo, stack-of-spirals sequence used to image the slice volume excited by the 3DTRF pulse.

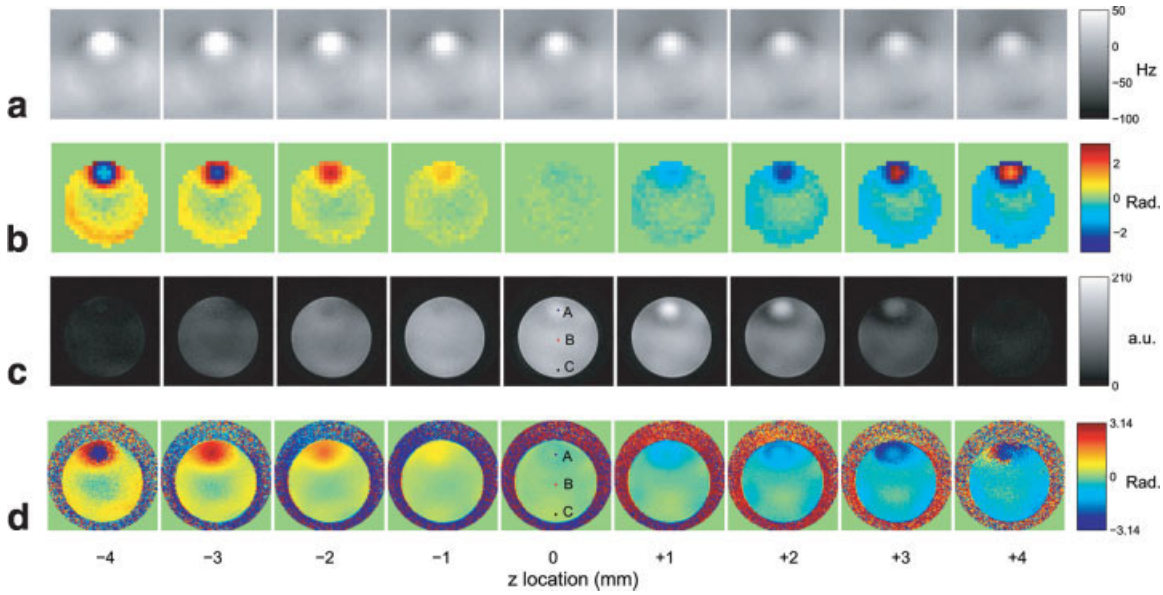

FIG. 7. **a:** Field maps on 1-mm subslices around the iso-center, revealing a "hot spot" of off resonance at the anterior phantom region (white). **b:** Desired phase pattern. **c,d:** Slice volume excited by the 3DTRF pulse, as imaged by the 3D sequence. The images provided evidence for fidelity of the slice-selective magnitude profile and good match between the desired and achieved phase pattern. Slice profiles at locations A–C are plotted in Fig. 9 (a.u.: arbitrary units).

the 3DTRF pulse using a 3D spin-echo "stack-of-spirals" sequence (Fig. 6). The sequence was identical to the 2D GRE sequence with 3DTRF pulse, except for an additional 180° pulse midway between the end of 3DTRF pulse and start of the spiral acquisition, a z gradient blip for phase-encoding (Fig. 6), and a shorter T_R (300 ms). The 180° pulse rewound the off-resonance-induced phase evolution, so that the magnetization pattern at the beginning of acquisition would be identical to that at the end of the 3DTRF pulse. In our experiment, the z gradient blip provided a 4-cm FOV in z, with 1-mm resolution. The 180° pulse selectively excited a 4-cm slab centered at the iso-center. 3D image of the slice volume was reconstructed from the 2D spiral images via inverse FFT along the phase-encoded z dimension.

Signal Recovery in Vivo

The goal of the human experiment was to show that the 3DTRF method was effective in the human head, in which the field variations were more complex than in the homogeneous phantom. For both the sinc and the 3DTRF pulses, we used the same GRE sequence as in the phantom experiment, except that we used only two spiral interleaves for image acquisition. The field map acquisition and 3DTRF pulse design were as described previously for the phantom experiment. We compared the brain images obtained with the sinc and 3DTRF pulses.

RESULTS

Signal Recovery in Phantom

Figure 7a shows estimated field maps interpolated to the desired pattern grid, for nine 1-mm subslices around the iso-center ($z = 0$). The maps revealed global main field inhomogeneity, while the anterior phantom region, superior to the metal attachment, exhibited significant frequency offsets (white "hot spot"). We estimated a map of the z-direction field gradient (Fig. 8a) via linear regression of the through-plane field variation. At the hot spot, the gradient was around -15×10^{-2} mT/m, a typical value measured in the ventral brain at 3 T.

The desired phase pattern (Fig. 7b, only the central nine subslices are shown) was subsequently derived from the differential field map and T_E. It contained rapid, approximately linear through-plane phase variation at the hot spot and minimal phase variation near the phantom center. Note that the pattern shown in Fig. 7b was masked by ROIs covering only the phantom. Finally, we formed the complex desired pattern by embedding that phase pattern in a

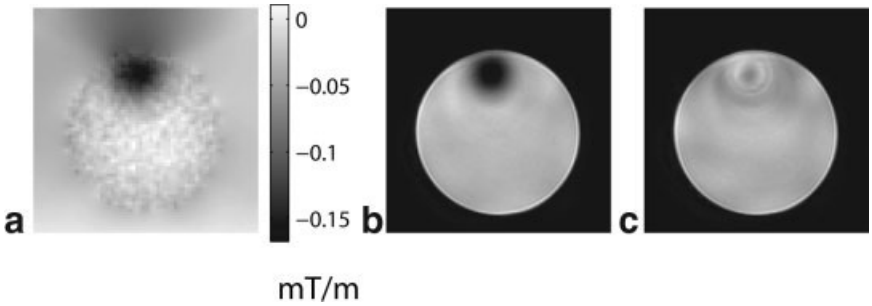

FIG. 8. **a:** Through-plane field gradient map at the iso-center, estimated from linear regression on field maps of phantom subslices. **b:** GRE image plagued by signal loss. **c:** GRE image with signal recovery using a 3DTRF pulse.

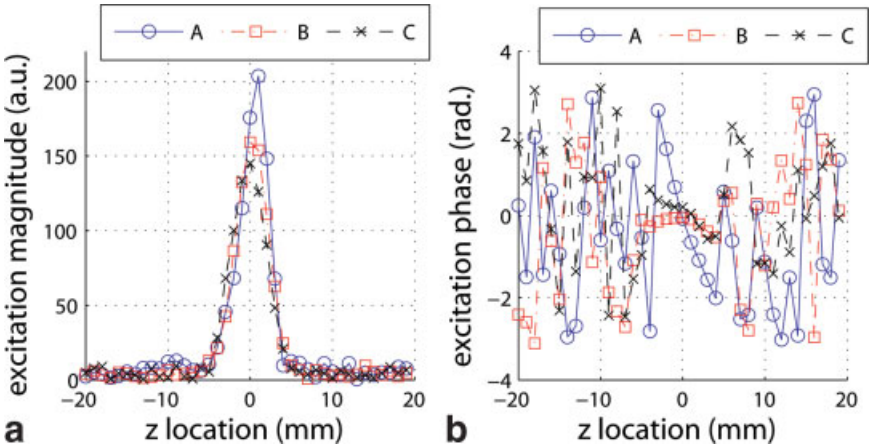

FIG. 9. Magnitude and phase of slice profiles at locations A–C in Fig. 7 (a.u.: arbitrary units). [Color figure can be viewed in the online issue, which is available at www.interscience.wiley.com.]

Gaussian profile with FWHM = 5 mm. Together with the field map, the desired pattern gave rise to 15.4-ms gradient waveforms (Fig. 2a) that produced the EV trajectory in Fig. 1. A complex RF pulse (Fig. 2b and c) was computed with CG in 257 s.

With the sinc pulse, signal loss was observed at the hot spot (Fig. 8b), predominantly caused by the through-plane field gradient (Fig. 8a). In contrast, the 3DTRF pulse excited the slice with signal recovered at the hot spot, while SNR at the remaining phantom regions was undiminished (Fig. 8c). Images of the slice volume, as captured by the 3D sequence (Fig. 7c (magnitude) and d (phase)), indicated that the 3DTRF pulse indeed excited a 3D precompensatory phase pattern as we intended. The imaged phase pattern (Fig. 7d) matched the desired one closely. The desired phase variation at the hot spot was achieved, whereas the phase through the phantom center remained coherent. Additionally, in the magnitude image of the slice volume, no excitation beyond the slice profile at iso-center was observed (not shown). The magnitude profile appeared centered and approximately Gaussian. Figure 9 shows the magnitude and phase profiles at three different in-plane locations (A–C), confirming fidelity of the excited slice volume.

One can observe, from the phantom images and profiles, that SNR uniformity was slightly compromised with the 3DTRF pulse. Nonuniformity occured particularly at regions with rapid in-plane transition in field map and desired phase. Nevertheless, slight SNR non-uniformity could generally be tolerated in fMRI.

Signal Recovery in Vivo

The structural brain image obtained at iso-center with a spoiled gradient recall (SPGR) sequence (Fig. 10a) contained structures (for example, thalamus and closing of the lateral ventricles) that indicated an inferior brain slice location. With sinc pulse excitation, the GRE image at the same location was plagued by signal loss (Fig. 10c). Signals from the inferior frontal cortex (IFC) were almost completely lost. Through-plane linear regression on the field maps of subslices resulted in a gradient map as shown in Fig. 10b, in which the regions of high gradient magnitudes were consistent with regions of signal loss. Figure 10d shows the

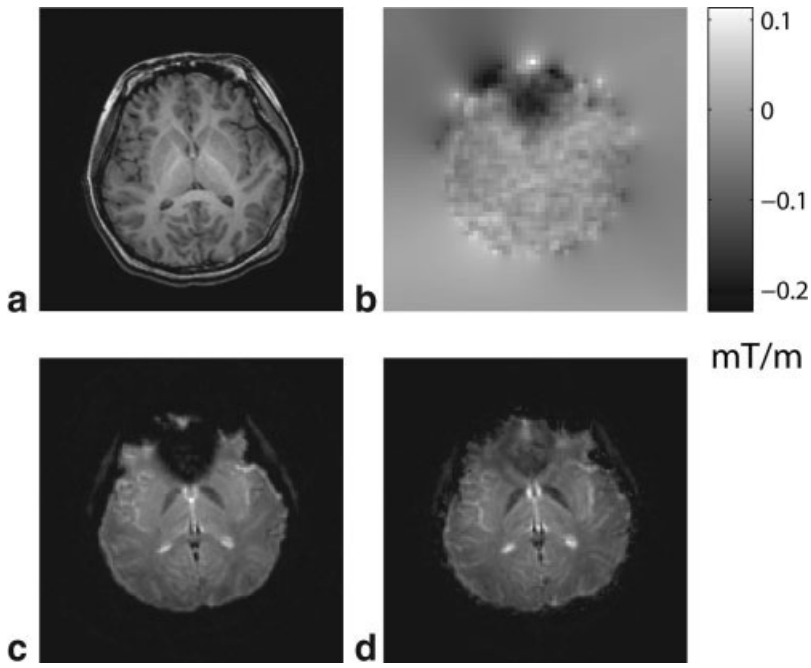

FIG. 10. **a:** SPGR image of an inferior brain slice. **b:** Through-plane field gradient map of the slice. **c:** GRE image plagued by signal loss. **d:** GRE image with signal recovery using a 3DTRF pulse.

image acquired using a 3DTRF pulse, computed in 260 s. Signals from the IFC was significantly recovered, while those from other brain regions remained mostly unaffected.

DISCUSSION

We have made several important advances to the original 3DTRF method reported in Ref. 11. We have introduced the new EV trajectory that enables accurate and fine slice selection. It avoids excitation sidelobes (11), and therefore obviates complimentary techniques for sidelobe removal, such as the asymmetric spin echo method (31). The EV trajectory, which is adaptive to the desired excitation pattern, is also efficient in sampling the desired pattern's spectrum in k-space, significantly reducing pulse length. We also adopt the iterative pulse design method, which allows frequency offset compensation for enhanced excitation accuracy. The pulse design process is greatly accelerated by the segmentation framework from the image reconstruction literature (21–24, 28). With orchestration of all the new components, we demonstrated successful signal recovery in a relatively thin (5 mm) slice in both phantom and inferior brain, using 3DTRF pulses that were only 15.4 ms long. Note that for the same slice thickness, the original design approach would require either very long pulses (>100 ms) (11) or multishot excitation (32). In our phantom experiment, we also showed good fidelity in the magnitude and phase of the excited slice volume, even in regions where the field was inhomogeneous.

The advances represent a major step toward a fully effective 3DTRF method for routine fMRI studies in loss-plagued brain regions. Indeed, the method is attractive compared to other popular "software methods" such as z-shimming (7) and thin slice acquisition (3) in terms of temporal resolution and SNR of the fMRI time series.

To see the advantage in fMRI temporal resolution, consider a time series acquired using a single-interleave 2D GRE sequence, covering a specified FOV in z with N slices. Relative to the baseline case with sinc pulse for slice selection, the 3DTRF method demands that the minimum sampling interval in the time series (ΔT_{min}) increases by $N \cdot s$, where s is the extra time needed for deploying a 3DTRF pulse in lieu of the sinc pulse. In contrast, for the same z coverage, n-step z-shimming or n-time slice thickness reduction results in an increase of ΔT_{min} by a *factor* of n. Therefore, given that s is short (12.2 ms in our experiments), the temporal resolution cost of the 3DTRF method can be much lower than that of z-shimming or slice thickness reduction.

The method also has a relative SNR advantage. Relative to the baseline SNR for a given slice thickness attainable in a loss-free brain region, a composite image formed from combining n subimages of $\Delta z/n$-thick slices has its SNR reduced by a factor of $\sqrt{n}$. A composite image formed from n z-shimming steps also has a lower average SNR, by a factor depending on the number of z-shimming steps and the step size. With the 3DTRF method, the baseline SNR can be preserved at image regions not plagued by signal loss, whereas SNR at loss-plagued regions can be comparable, provided that signal recovery there is nearly complete. However, SNR uniformity across image can be affected slightly, even at regions that are originally not plagued by signal loss (see Fig. 8).

The currently proposed 3DTRF method is effective in signal recovery under two conditions. First, the target phase pattern must be smooth in the in-plane dimensions because of the scarcity of phase-encoding locations. Recovery efficacy is limited when there are multiple regions of signal loss (for example, on a slice with loss caused by *both* the air-filled middle ears and the sinuses). One might be tempted to add phase-encoding locations to pursue the necessary in-plane excitation variability. Unfortunately, additional phase-encoding, implemented via extra pulse segments appended to the beginning of the original pulse, becomes increasingly marred by the off-resonance dephasing up to the pulse end. As a result, the addition become less and less "usable" by CG in approximating the desired pattern. This "phase-encoding ceiling" exists even though the dephasing is modeled in the design and accounted for. The ceiling poses a limit on the in-plane variability that a 3DTRF pulse can possibly render.

Note that the dephasing that causes the ceiling is proportional to both the phase accumulation time and the frequency offset magnitude. Large frequency offsets impose low phase-encoding ceilings, potentially leading to insufficient in-plane encoding for successful recovery. Therefore, the second critical condition for successful recovery is that the magnitude of frequency offsets is not too large (below 75 Hz at 3 T). Large frequency offsets are devastating to the in-plane excitation accuracy, although the effect in the z direction is minimal.

Strategies to break through the phase-encoding ceiling will enable signal recovery at multiple image regions in the presence of large frequency offsets. Any prospective approach to the 3DTRF method must provide encoding capability that is less vulnerable to dephasing. Toward this goal, parallel excitation can potentially be beneficial. Alternatively, successful signal recovery with the current design approach can be accomplished over the entire brain if frequency offsets are somehow reduced. The localized intraoral and external shimming methods (14–16) were demonstrated to be effective in improving overall field homogeneity. The 3DTRF method, if applied in concert with those shimming techniques, could potentially provide the intricate corrections that gross localized shimming fails to do.

APPENDIX

Histogram-Based, Least-Square Time Segmentation

We summarize, in the segmentation framework for pulse design acceleration, the *histogram-based, least-square time segmentation approach* (28) in deriving $p_{il}, i = 0, \ldots, N_s - 1$, and $q_{lj}, j = 0, \ldots, N_t - 1$. Let us define uniform time samples $\tau_l, l = 1, \ldots, L$, within the pulse duration, and form L temporal segments, $p_{il} = e^{\imath\omega(\mathbf{r}_i)\tau_l}, l = 1, \ldots, L$. Now, the goal is to determine temporal interpolator, q_{jl}, that we pair up with the lth segment. Suppose the histogram of the field map, $\Delta\omega(\mathbf{r}_i)$, has K bins, and ω_k and h_k are the center and occurrence frequency of the kth bin.[3]

[3]Occurrence count of the frequency offset at $\mathbf{r}_i$ could be weighted by the error weighting, W_i.

Define matrices

$$\mathbf{E} = \{e_{kj}\}, \qquad e_{kj} = e^{\imath\omega_k t_j}, \qquad [11]$$

$$\tilde{\mathbf{P}} = \{\tilde{p}_{kl}\}, \qquad \tilde{p}_{kl} = e^{\imath\omega_k \tau_l}, \qquad [12]$$

$$\tilde{\mathbf{Q}} = \{q_{lj}\}, \qquad [13]$$

$$\mathbf{H} = diag\{h_k\}, \qquad [14]$$

where $i = 0, \ldots, N_s - 1, j = 0, \ldots, N_t - 1, k = 1, \ldots, K$, and $l = 1, \ldots, L$. The L temporal interpolators can be computed by the following histogram-weighted least-square formula:

$$\tilde{\mathbf{Q}} = (\tilde{\mathbf{P}}'\mathbf{H}^2\tilde{\mathbf{P}})^{-1}\tilde{\mathbf{P}}'\mathbf{H}\mathbf{E}. \qquad [15]$$

The lth row in $\mathbf{Q}$, $q_{lj}, j = 0, \ldots, N_t - 1$, is the temporal interpolator to be paired with segment $p_{il}, i = 0, \ldots, N_s - 1$. The L pairs are to be used in the segmentation framework. Readers should refer to Ref. (28) for elaboration on this approach and alternative options.

REFERENCES

1. Lipschutz B, Friston KJ, Ashburner J, Turner R, Price CJ. Assessing study-specific regional variations in fMRI signal. Neuroimage 2001; 13:392–398.
2. Deichmann R, Gottfried JA, Hutton C, Turner R. Optimized EPI for fMRI studies of the orbitofrontal cortex. Neuroimage 2003;19:430–441.
3. Merboldt KD, Finsterbusch J, Frahm J. Reducing inhomogeneity artifacts in functional mri of human brain activation-thin sections vs gradient compensation. J Magn Reson 2000;145:184–191.
4. Yoo SS, Guttmann CR, Panych LP. Multiresolution data acquisition and detection in functional MRI. Neuroimage 2001;14:1476–1485.
5. Chen NK, Dickey CC, Yoo SS, Guttmann CR, Panych LP. Selection of voxel size and slice orientation for fMRI in the presence of susceptibility field gradients: application to imaging of the amygdala. Neuroimage 2003;19:817–825.
6. De Panfilis C, Schwarzbauer C. Positive or negative blips? The effect of phase encoding scheme on susceptibility-induced signal losses in EPI. Neuroimage 2005;25:112–121.
7. Glover GH. 3D z-shim method for reduction of susceptibility effects in BOLD fMRI. Magn Reson Med 1999;42:290–299.
8. Song AW. Single-shot EPI with signal recovery from the susceptibility-induced losses. Magn Reson Med 2001;46:407–411.
9. Heberlein KA, Hu X. Simultaneous acquisition of gradient-echo and asymmetric spin-echo for single-shot *z*-shim: Z-SAGA. Magn Reson Med 2004;51:212–216.
10. Cho Z, Ro Y. Reduction of susceptibility artifact in gradient-echo imaging. Magn Reson Med 1992;23:193–200.
11. Stenger VA, Boada FE, Noll DC. Three-dimensional tailored RF pulses for the reduction of susceptibility artifacts in T_2^*-weighted functional MRI. Magn Reson Med 2000;44:525–531.
12. Glover GH, Law CS. Spiral-in/out BOLD fMRI for increased SNR and reduced susceptibility artifacts. Magn Reson Med 2001;46:515–522.
13. Li TQ, Takahashi A, Wang Y, Mathews V, Glover GH. Dual-echo spiral in/in acquisition method for reducing magnetic susceptibility artifacts in blood-oxygen-level-dependent functional magnetic resonance imaging. Magn Reson Med 2006;55:325–334.
14. Wilson JL, Jenkinson M, Jezzard P. Optimization of static field homogeneity in human brain using diamagnetic passive shims. Magn Reson Med 2002;48:906–914.
15. Hsu JJ, Glover GH. Mitigation of susceptibility-induced signal loss in neuroimaging using localized shim coils. Magn Reson Med 2005;53: 243–248.
16. Wong EC, Mazaheri Y. Shimming of the inferior frontal cortex using an external local shim coil. In: Proceedings of the 12th Annual Meeting of ISMRM, Kyoto, 2004, p. 520.
17. Katscher U, Börnert P, Leussler C, van den Brink JS. Transmit SENSE. Magn Reson Med 2003;49:144–150.
18. Zhu Y. Parallel excitation with an array of transmit coils. Magn Reson Med 2004;51:775–784.
19. Pauly JM, Nishimura DG, Macovski A. A *k*-space analysis of small-tip-angle excitation. J Magn Reson 1989;81:43–56.
20. Yip CY, Fessler JA, Noll DC. Iterative RF pulse design for multidimensional, small-tip-angle selective excitation. Magn Reson Med 2005;54:908–917.
21. Noll DC. Reconstruction techniques for magnetic resonance imaging. Ph.D. thesis, Stanford University, CA, 1991.
22. Noll DC, Meyer CH, Pauly JM, Nishimura DG, Macovski A. A homogeneity correction method for magnetic resonance imaging with time-varying gradients. IEEE Trans Med Imaging 1991;10:629–637.
23. Man LC, Pauly JM, Macovski A. Multifrequency interpolation for fast off-resonance correction. Magn Reson Med 1997;37:785–792.
24. Sutton BP, Noll DC, Fessler JA. Fast, iterative image reconstruction for MRI in the presence of field inhomogeneities. IEEE Trans Med Imaging 2003;22:178–188.
25. Mansfield P, Howseman AM, Ordidge RJ. Volumar imaging using NMR spin echos: echo-volumar imaging (EVI at 0.1 T. J Phys E Sci Instrum 1989;22:324–330.
26. Oelhafen M, Pruessmann KP, Kozerke S, Boesiger P. Calibration of echo-planar 2D-selective RF excitation pulses. Magn Reson Med 2004;52: 1136–1145.
27. Fessler JA, Sutton BP. Nonuniform fast Fourier transforms using min-max interpolation. IEEE Trans Signal Proc 2003;51:560–574.
28. Fessler JA, Lee S, Olafsson VT, Shi HR, Noll DC. Toeplitz-based iterative image reconstruction for MRI with correction for magnetic field inhomogeneity. IEEE Trans Signal Proc 2005;53:3393–3402.
29. Schneider E, Glover GH. Rapid in vivo proton shimming. Magn Reson Med 1991;18:335–347.
30. Fessler JA, Desmond Yeo, Noll DC. Regularized fieldmap estimation in MRI. In Proceedings IEEE Intl Symp Biomed Imaging, 2006. p 709.
31. Noll DC, Stenger VA. A 3D tailored RF pulse asymmetric spin-echo pulse sequence for susceptibility correction in functional MRI. In: Proceedings of the 10th Annual Meeting of ISMRM, Honolulu, 2002.
32. Stenger VA, Boada FE, Noll DC. Multishot 3D slice-select tailored RF pulses for MRI. Magn Reson Med 2002;48:157–165.